Nonreciprocal multibody interactions activate liquid state of acoustically levitated particle ensembles

Nina M. Brown * and Heinrich M. Jaeger
James Franck Institute, University of Chicago, Chicago, Illinois, USA
and Department of Physics, University of Chicago, Chicago, Illinois, USA

(Received 30 July 2026; accepted 8 October 2026; published 30 October 2026)

Nonreciprocal forces are often a consequence of asymmetry in the properties of the interacting objects. However, even if all objects are identical and isotropic, and the pairwise interactions between two objects are completely reciprocal, nonreciprocal forces can still appear when an arrangement of many objects breaks configurational symmetry in the presence of nonpairwise, multibody interactions. Here, we demonstrate that such emergent nonreciprocity can activate a particle ensemble to behave like a liquid, albeit with unique traits. In our experiments, passive microspheres are acoustically levitated in air, where they form a freely floating monolayer containing up to a couple hundred particles and collectively behave like a two-dimensional liquid droplet. The particles interact via nonreciprocal multibody forces that arise from the combination of acoustic scattering and sound-induced viscous microstreaming. We find that these forces drive superdiffusive particle motion with non-Gaussian tails in the particles' speed distribution. Using probes that reach laterally into the levitation plane, we perform liquid pendant drop and pinch-off experiments. Compared to ordinary liquids, the droplets are found to have a kinematic viscosity similar to that of water, but in combination with an extremely low interfacial tension. The pinching-off is driven by nonreciprocity-induced active fluctuations and exhibits the self-similar double-cone neck profile seen also in liquid nanojets close to rupture, however, here characterized by power law behavior with a scaling exponent that is anomalously small.

DOI: 10.1103/vdq4-r1cc

I. INTRODUCTION

In systems ranging from active matter to robotic metamaterials to particle-laden plasmas, nonreciprocal forces are known to induce dynamics and spatiotemporal patterns not observed with conservative interactions [1–4]. Nonreciprocal forces typically arise from an explicit symmetry breaking, either because of an asymmetry in the properties of the interacting species or objects [5], or because the nonreciprocity has been programmed into the interactions, as in robotic swarms or metamaterials [3]. Nonreciprocal interactions can also occur among a single species or identical objects if there is a front-back asymmetry, such as a limited vision cone or a trailing wake [6–8]. A rather different situation occurs in systems comprising identical objects with pairwise forces that obey reciprocity. In this case, nonreciprocal forces require nonpairwise, i.e., multibody interactions. This has been studied, in particular, for multibody interactions mediated by a field. Examples include active particles in a temperature or chemical concentration field [9], and passive particles in an optical [10–12] or a sound [13–16] field. When asymmetries in the spatial configuration of the particles distort the field, this then can lead to net momentum flux and generate movement. Such emergent nonreciprocity tends to amplify spatial particle fluctuations via positive feedback. An intriguing outcome is that even if all particles individually are passive and nonmotile, activity can be induced by nonreciprocal multibody interactions. In small groups of identical passive, isotropic particles, this induced activity has been found to enable collective propulsion and also limit cycles [10,11,13,16]. In larger ensembles, it has been observed to drive intermittent local rearrangements that, with increasing level of activity, destroy ordered particle configurations and eventually give way to a liquidlike state [15]. However, the macroscale properties of such a nonreciprocal liquid have not yet been studied.

Here, we report on experiments that enable us to extract properties such as an effective line tension and viscosity from two-dimensional (2D) particle liquids activated by nonreciprocal multibody interactions. We use acoustic levitation in air to lift microparticles against gravity and self-assemble them into monolayer configurations in a well-defined levitation plane. Within that plane, the particles interact via forces generated by an intense ultrasound field, forming 2D ensembles that behave like liquid droplets. The experiments are enabled by a unique setup in which levitating particle ensembles can be manipulated with probes that reach into an acoustic cavity [17,18]. Suitably designed probes make it possible not only to generate uniform acoustic potential gradients within the levitation plane, but also to apply controlled tensile stress to the droplets. During the experiments, the motion of all particles can be tracked with high-speed video.

*Contact author: nmbrown@uchicago.edu

Published by the American Physical Society under the terms of the Creative Commons Attribution 4.0 International license. Further distribution of this work must maintain attribution to the author(s) and the published article's title, journal citation, and DOI.

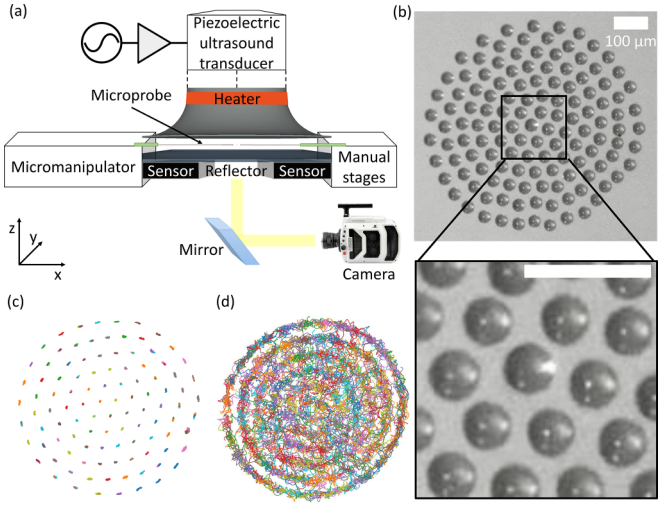


FIG. 1. Experimental realization of an acoustically levitated, 2D liquid of identical granular particles. (a) Sketch of the setup, including micromanipulators with probes that reach into the acoustic cavity to perturb levitating particle liquid droplets. (b) Snapshot from high-speed video of a droplet of microparticles (top), with enlarged central section (bottom). Scale bar: 100 μm. (c) Particle trajectories over 0.1 s within a droplet at a relatively low sound pressure of $p_{ac} = 3880$ Pa. (d) Same as panel (c) but for $p_{ac} = 5920$ Pa.

II. ACOUSTIC LEVITATION EXPERIMENTS

Figure 1(a) shows a sketch of our experimental setup. A piezoelectric ultrasound transducer (40.45 kHz) drives an aluminum Langevin horn positioned half a sound wavelength ($\lambda = 8.5$ mm) above a reflecting glass surface, causing a standing wave to form. This creates an acoustic resonance cavity with a low-pressure zone at the central nodal plane where particles can be levitated against gravity. Our experiments use monodisperse polystyrene spheres with diameter $d = 40.4\ \mu\text{m} \ll \lambda$; i.e., we operate deep in the Rayleigh scattering limit. We control the acoustic energy density [19]

$$E_0 = \tfrac{1}{2}\beta_0 p_{ac}^2 \tag{1}$$

in the cavity by monitoring it with ultrasound pressure sensors, adjusting the amplitude of the signal applied to the ultrasound transducer, and stabilizing the temperature of the horn [17]. Here, β_0 is the compressibility of the levitation medium (air), and p_{ac} is the rms amplitude of the oscillating sound pressure. Experimental values of p_{ac} are estimates of the maximum pressure in the levitation plane determined from measurements of the system combined with finite element analysis simulations (see Appendix A). The levitating particle rafts are imaged from below with a high-speed camera at rates of 5000–10 000 frames per second [Fig. 1(b)].

Acoustic scattering interactions arise when a wave scattered by levitated particles interferes with the incident wave. Between two solid spheres, this results in a force between particles that is attractive within the levitation plane but repulsive if a particle approaches from a perpendicular direction. At close range, the attractive interaction between two identical spheres follows the form [19]

$$F_{sc}(r) \sim -\frac{E_0 d^6}{r^4}. \tag{2}$$

An ensemble of identical spheres forms a quasi-2D raft structure bound by acoustic scattering.

The particle separation within levitating ensembles results from the balance between attractive scattering forces and repulsive forces from sound-induced microstreaming. This balance is controlled by the Stokes number $\Omega = \omega d^2/(4\nu) = (d/\delta_\nu)^2/2$ [15,19]. Here, ω is the sound frequency, ν is the kinematic viscosity of the levitating medium (air), and $\delta_\nu = \sqrt{2\nu/\omega}$ is the characteristic thickness of the viscous boundary layer surrounding the particles, which effectively generates an enlarged hydrodynamic particle radius. For our particle size and sound frequency, $\delta_\nu \approx 11$ μm. This gives $\Omega \simeq 6.6$ and leads to a center-to-center spacing of $a = 1.26d$ between particles in the levitation plane. Since the competing forces are both proportional to the sound intensity given by Eq. (1), this particle spacing is independent of E_0 or, equivalently, p_{ac} [19]. The functional form of the microstreaming repulsion between a pair of identical spheres is, to good approximation, an exponential decay over a characteristic separation distance δ_ν [15]. Thus, particles experience short-ranged repulsion and long-ranged attraction.

For just two identical spheres, this interaction is conservative and reciprocal, resulting in a stable dimer with fixed steady-state separation. However, when more particles are added, nonconservative multibody interactions can drive a system away from stable, static configurations and introduce activity. This occurs already in clusters of three spheres, where breaking of inversion symmetry introduces nonreciprocal three-body forces, i.e., a net momentum flux that can drive propulsion or sustain oscillatory limit cycles [16]. In larger systems, nonreciprocal multibody interactions were found to destabilize ordered configurations by reducing the resistance to shear, resulting in intermittent, stringlike particle rearrangements that increase in frequency with acoustic energy density E_0 until they result in a liquidlike state [15].

Both scattering and microstreaming can contribute to this nonreciprocity, but simulations show that for particles in the Rayleigh regime, as in our systems, contributions from microstreaming dominate [15,16]. In all of these cases, the particles are individually passive and far too large to experience thermal fluctuations. The activity therefore is a direct result of nonreciprocity that emerges from field-mediated multibody interactions when local particle configurations break spatial symmetry. As E_0 increases, the strength of the nonconservative, nonreciprocal contribution to the interactions increases as well, eventually enabling continuously sustained particle fluctuations. Importantly, in the experiments presented here, particles do not experience significant excursions away from the levitation plane. There are known instabilities in slightly detuned cavities that can cause motion of levitated objects [20,21], but this motion is typically in the direction perpendicular to the levitation plane.

Experimental methods

The experimental setup is pictured in Fig. 1(a). We drive a piezoelectric ultrasound transducer (Steiner & Martins

SMBLTD45F40H) with a 40.45–40.7 kHz sinusoidal signal from a function generator (BK Precision 4052) and a high-voltage amplifier (A.A. Lab Systems A-301 HS). The transducer is attached to a custom-machined aluminum horn, which amplifies the signal (horn design from Ref. [22]). The horn is heated to a constant temperature of 35 °C to maintain consistent resonance properties. The bottom edge of the horn is approximately one half-wavelength ∼4.2 mm from a transparent reflector plate. The reflector is made of transparent glass and coated with indium tin oxide (ITO) to minimize the influence of charging and electrostatic forces. A mirror is placed below the reflector at a 45° angle, and a Phantom v2512 high-speed camera is used to capture experiments from below and observe the nodal plane of the cavity. A Navitar Resolv4K lens is used to achieve a maximum resolution of approximately 2.5 μm per pixel at a working distance of 6.5 cm. The acoustic pressure in the system is monitored by several low-profile ultrasound sensors (PUI Audio SMUT-1040K-TT) placed below the reflector. A feedback control system with the ultrasound sensors and the function generator maintains a constant acoustic pressure in the cavity during experiments, as described in Ref. [17], which helps to accommodate small changes in the laboratory environment. The setup is partially enclosed in an acrylic box and located atop a passive vibration isolation platform (ThorLabs IsoPlate PTT900600).

Polystyrene spheres with diameter $d = 40.4 \pm 0.9$ μm were levitated in these experiments (microParticles GmbH). These particles are coated with fumed silica nanoparticles (Evonik Aeroxide AluC) to prevent contact adhesion from van der Waals (vdW) forces; this is described in Ref. [23]. To avoid the influence of electrostatic forces, levitated particles and microprobes were discharged prior to each experiment with a soft x-ray photoionizer (Hamamatsu L12645). Microprobes with a width of approximately 200 μm are used to perturb the system; these were manufactured using a continuous liquid interface production method [24]. A motorized micromanipulator (Eppendorf Patchman NP2) is used to control microprobe motion.

All image processing and data analysis were performed in PYTHON; raft and microprobe positions were obtained from experimental images using the Segment Anything Model [25]. Particle positions and tracks were determined using the trackpy PYTHON package [26]. Droplet center-of-mass motion was removed from the particle positions so as to examine the relative motion of particles within the droplet. Fitting of pendant drop profiles utilized a custom modified version of the OPENDROP software [27,28].

III. ACOUSTICALLY DRIVEN ACTIVE LIQUID STATE

As the sound pressure p_{ac} is increased beyond a certain level, in-plane particle fluctuations due to nonconservative forces drive a levitating particle ensemble from a nearly quiescent, highly ordered state to a state of constant particle movement, resembling a liquid droplet [15]. Figure 1(b) shows a snapshot of such a droplet, while panels (c) and (d) show individual particle trajectories for a comparable particle raft over 0.1 s at different p_{ac}. Video of the experiments portrayed in panels (c) and (d) can be seen in Movie S1 of the

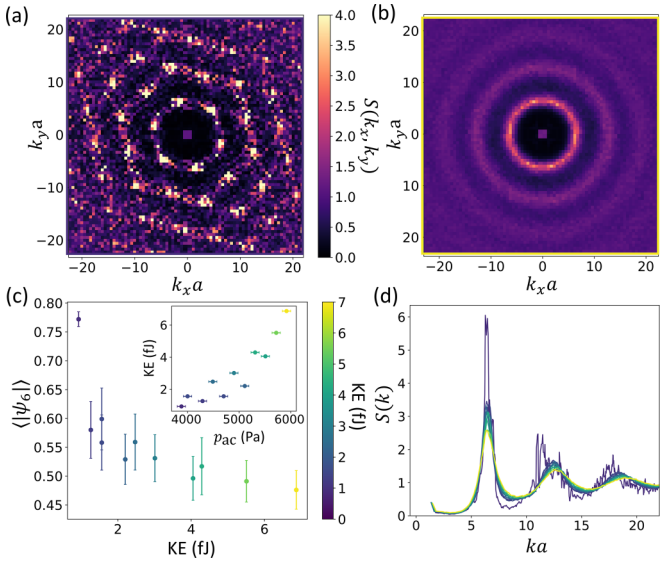


FIG. 2. Structural characterization of 2D liquid droplets. (a) Static structure factor $S(k_x, k_y)$ at the lowest sound pressure probed (3880 Pa). (b) Same as panel (a) but at the highest pressure (5920 Pa). (c) Orientational order parameter $|\psi_6|$ and average KE of particles within droplets as a function of acoustic pressure p_{ac} (error bars: standard deviation over time of mean $|\psi_6|$). Color bar also applies to panel (d). (d) Static structure factor magnitude $S(k)$ vs wave number ka for droplets with different particle kinetic energy.

Supplemental Material [29]. As the liquidlike state is entered, structural ordering first diminishes in the outer layers of the droplet, where there are more local packing defects relative to the droplet core due to the droplet's round boundary.

This change in behavior is reflected in the static structure factor $S(k)$, shown in Figs. 2(a) and 2(b), plotted as a function of wave number $k_x a$, $k_y a$. For a solidlike droplet at low p_{ac}, $S(k_x, k_y)$ displays the hexagonal structure associated with a close-packed particle configuration, while for higher pressure this pattern turns into circular rings, indicating a complete lack of orientational order. The loss of orientational order with increasing p_{ac} can be quantified by the orientational order parameter $|\psi_6|$ (see Appendix B), which is plotted in Fig. 2(c). As $|\psi_6|$ decreases, the same plot shows how the average kinetic energy (KE) per particle increases rapidly with p_{ac}. Kinetic energy data are plotted both for increasing and decreasing p_{ac}. The variation in the data is due to a slight change in the experimental environment over time; closed-loop feedback control of the acoustic pressure helps to mitigate this, but it is difficult to eliminate entirely. In the following, we take this kinetic energy as a proxy for a particle-motion-based effective temperature of the droplets.

Due to the small system size, we cannot observe long-range correlations. However, we observe the loss of orientational order at short range, indicating a transition to a liquid state. This suggests increasing dislocation and disclination densities, as seen in both equilibrium and nonequilibrium 2D systems [30], but further study is needed to fully characterize this phase transition. Prior work has identified an intermediate state with intermittent stringlike dynamics [15]. Here, we focus on descriptions of the droplet's phase through structural parameters.

In three-dimensional (3D) systems, the Hansen-Verlet rule classifies a material as transitioning from a solidlike to a liquid state once the first peak of $S_{\max}(k) > 2.85$ [31]. In 2D, the equivalent criterion is $S_{\max}(k) \gtrsim 4$–5 [32], where different interparticle interactions result in slightly different critical values, e.g., 4.4 for a plasma [33] and 4.7 for a Lennard-Jones fluid [34]. In our data, the first peak of $S(k)$ decreases from 6.0 very quickly to 3.5 and then to 2.6 with increasing p_{ac} [Fig. 2(d)]. Comparing with the critical values for other 2D systems, this suggests that all droplets tested should be in a liquid state except for the droplet at the lowest p_{ac} value. However, the height of the first peak of $S(k)$ in systems with small number of particles N is known to be lower than for large N [35], so an exact criterion for this system should not be assumed from this data. Our rafts, with $N \sim 100$, enter their liquid state at the low end of the pressure range shown in Fig. 2(d). This is supported by the fact that at $p_{\text{ac}} = 3880$ Pa, where the first peak of $S(k) = 6.05$, the hexagonal pattern in $S(k_x, k_y)$ still is dominant. Furthermore, splitting of the second peak of $S(k)$ is expected once a freezing transition is crossed; similar behavior is expected for the radial distribution function $g(r)$ [32]. At the lowest p_{ac}, the second peak of $S(k)$ appears to exhibit two major subpeaks, while curves for higher p_{ac} do not. This can be seen more clearly in the radial distribution function (Fig. 7). We find closely related trends with acoustic pressure between $S(k)$ and $g(r)$ (Appendix B).

Speed distributions and anomalous diffusion. Figure 3 shows results from tracking individual particle motion inside a droplet of $N = 106$ particles at different p_{ac}. The parameters measured in Fig. 3 are common to all N probed. The speed [panels (a) and (b)] and displacement [panel (c)] distributions differ from the thermal case by exhibiting wider tails. To highlight this, in Fig. 3(b) we plot the speed distributions against $|v|^{3/2}$. An exponential distribution $P \sim e^{-x^k}$ with exponent $k = 3/2$ is seen to provide a remarkably good fit not only to the high-speed tails but also at lower speeds closer to the peak, i.e., the average KE. Still, an even better match is achieved with a slightly smaller exponent. In the inset of Fig. 3(b), the same data are plotted on log scales as the natural log of the normalized probability $\overline{P} = P/P_{\max}$ versus normalized velocity $\overline{v} = (v - v_{\text{avg}})/v_{\text{avg}}$ for $v > v_{\text{avg}}$. The slopes on this plot represent the exponent k. From a best fit to each curve, we obtain $k = 1.34 \pm 0.06$ (mean $\pm$ standard deviation). This lies in contrast to a thermally activated system, which follows a Gaussian distribution ($k = 2$).

Exponents $k < 2$ are seen in some other granular systems. For a thermally heated granular gas with collisions, it is predicted that the tail of the velocity distribution goes like $k = 3/2$ [36]. However, our distributions differ from a Gaussian over most of their width, not just the tails. Experiments of some granular systems have also demonstrated distributions that have $k = 3/2$ or other deviations from a Gaussian that persist across the full range of velocities rather than just in the tail [37,38]. Alternate theories have tried to reconcile this, incorporating features such as randomly varying coefficients of restitution [39] and negative friction [40]. In our experiments, the hard-sphere particles are surrounded by a soft shell formed by a repulsive viscous boundary layer set up by microstreaming flows [16,19]. Random values for the coefficient of restitution might then be a consequence of particle collisions at different impact parameters, or perhaps the nonreciprocal nature of the interactions results in an effective negative friction. If a particle moves away from a stable position within a quiescent particle raft (low p_{ac}), it experiences a nonrestoring force in the direction of displacement that encourages shear [15]; this could potentially be modeled as a type of negative friction. We imagine that the same principles apply to our experiments, which are at higher p_{ac} where stronger interactions generate fluctuating configurations that are constantly changing.

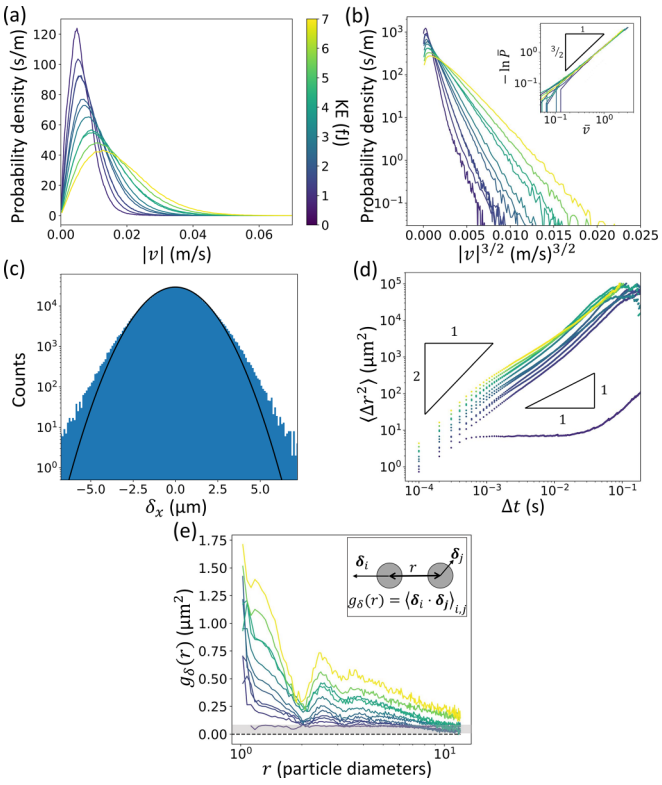


FIG. 3. Statistics of particle motion for a levitated granular droplet ($N = 106$) at different p_{ac}. (a) Speed distributions for the droplet, colored by mean particle kinetic energy. Color bar also applies to panels (b) and (d)–(f). (b) Speed distributions vs $|v|^{3/2}$, y axis on a log scale. (b) Inset: Natural log of the normalized distribution tails $\overline{P}$ vs normalized velocity $\overline{v}$, on a log-log scale. Triangle drawn with slope 3/2. (c) Distribution of particle displacements in one direction for a high-pressure experiment ($p_{\text{ac}} = 5920$ Pa), y axis on a log scale. Line is a Gaussian fit. (d) Mean square displacement vs time on a log-log scale. Triangles are drawn with slopes 1 and 2. (e) Displacement correlation function $g_\delta(r)$ vs r, x axis on a log scale. Gray shaded area represents noise level. (e) Inset: Schematic of $g_\delta(r)$ for two particles.

Clear deviations from the Gaussian behavior expected for thermal motion are also seen in the particle displacement distributions. Figure 3(c) shows a representative histogram of displacements parallel to the x axis between sequential imaging frames ($\Delta t = 1/10\,000$ s). Thus, particles within an acoustically levitated liquid droplet are more likely to move at high velocities (large displacements) relative to molecules comprising a noninteracting thermal fluid. This translates into superdiffusive behavior, whereby the mean square displacement (MSD) increases with time faster than linear [Fig. 3(d)].

This superdiffusion is typical for systems of active particles [41,42], living organisms [43], and other systems with nonreciprocal forces like particle-laden ("dusty") plasmas [44,45]. The MSD of the solidlike droplet probed displays an initial steeper slope, which quickly falls off to a flat line; this suggests that the particles experience small fluctuations on a short timescale, but are caged in a lattice configuration. Once in a liquid state, even at the lowest effective temperatures, particles do not appear to experience significant caging. This is consistent with the lack of caging observed for particle rafts in an intermediate state that displays intermittent dynamics [15].

To further check for vestiges of the stringlike collective particle displacements observed as intermittent disruptions of the solidlike state at lower sound pressure [15], we define a correlation parameter for simultaneous displacement between two particles as

$$g_\delta(r) = \langle \boldsymbol{\delta}_i \cdot \boldsymbol{\delta}_j \rangle_{i,j}. \tag{3}$$

Here, $\boldsymbol{\delta}_i$ is the displacement vector of particle i, and the average is taken over all particle pairs in a droplet. This value is then averaged across a whole experiment. A schematic is drawn in the inset of Fig. 3(e). This quantifies the degree to which a particle's direction of motion is correlated with that of particles a distance r away. Figure 3(e) shows $g_\delta(r)$ averaged over the course of each experiment. The dark purple curve that remains relatively flat represents the solidlike droplet. Each of the curves for the liquidlike droplets exhibits peaks at the first two neighbor positions before gradually decreasing with a trend that appears logarithmic. Even when particles are closer than their mean spacing ($r < 1.26d$), g_δ tends to be positive. Within these droplets, one particle that moves close to another may cause the other particle to move away, but the first particle does not necessarily move in the opposite direction; this may be a result of the high velocity required for particles to be in closer proximity than the distance imposed by their viscous boundary layers. In the solidlike limit, $g_\delta(r)$ is small but positive, suggesting slight correlations; this is likely a result of minute errors in particle tracking, and we take this value as a noise floor.

For contrast, we performed molecular dynamics (MD) simulations of a system in which the nonreciprocal multibody interactions are replaced by simple pairwise interactions in the presence of thermal noise. These simulations included a repulsive pairwise Yukawa potential, radial confinement, and Brownian fluctuations; simulated particles form a round Wigner crystal similar in structure to the experimental droplets but with only pairwise interactions (Appendix C). In these simulations, there was very little correlation of particle displacements beyond close-range negative correlations for strong interparticle repulsion, and any correlations fell quickly to zero (Fig. 8). In the experimental system, therefore, the nonreciprocal multibody interactions are important for driving correlated particle motion.

Experiments discussed in the remainder of this article were performed with droplets in a liquidlike state.

IV. PENDANT DROPLETS AND INTERFACIAL TENSION

Pendant drop experiments are commonly used to extract the surface tension γ of liquids. In such experiments, a small droplet of the liquid hangs from a surface or needle and deforms under the influence of gravity, which makes it possible to extract γ from analyzing the droplet profile. The droplet shape is determined by the balance of surface tension γ and gravity, which is expressed by the Bond number Bo defined as

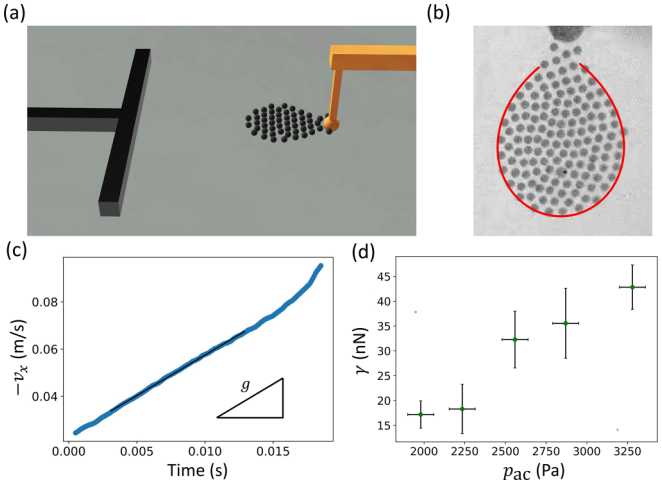


FIG. 4. Pendant drop experiments were performed to quantify the interfacial tension of this granular liquid. (a) Experiment diagram. (b) Experiment image with drop profile drawn (red). (c) Mean particle velocity while droplet is "falling" between the two probes. A line is fit to a segment of the data; triangle shows slope (droplet acceleration). (d) Surface tension vs effective temperature parameter p_{ac}.

$$\mathrm{Bo} = \frac{\Delta\rho g R_0^2}{\gamma}. \tag{4}$$

Here, $\Delta\rho$ is the difference in density between the droplet and the external medium (often air), g is gravitational acceleration, and R_0 is the radius of the droplet's bulb. The expression for the Bond number turns out to be the same for the 2D case, but now $\Delta\rho$ refers to area density and γ becomes a line tension (see Appendix D). By subjecting a levitating droplet to a uniform force field that mimics gravity, we can therefore extract the Bond number from measurements of the droplet shape, which provides access to the line tension.

A side view schematic of our experimental setup is shown in Fig. 4(a). We insert two microscale probes into the acoustic cavity to carefully alter the acoustic field within the (horizontal) levitation plane and interact with levitated particles [17,18]. A levitating droplet of particles is pinned in place by a probe with a large sphere (180 μm diam.) that reaches from above into the levitation plane [orange in Fig. 4(a)]. We then move a larger, T-shaped probe within the levitation plane toward the droplet [black in Fig. 4(a)]. The large size of the probe bodies compared to that of the particles implies that the probes generate a force field that attracts the small particles via scattered sound [17]. As the T-shaped probe approaches laterally, the droplet experiences increasing attraction, causing it to deform. A sample pendant drop is shown in Fig. 4(b). Eventually, the droplet detaches and horizontally "falls" onto the T-shaped probe (see Movie S2 of the Supplemental Material [29]). Tracking the center-of-mass motion of the droplet during this "falling" stage, we can determine the effective acceleration g needed for calculating Bo in Eq. (4).

Figure 4(c) shows a representative plot of droplet velocity versus time after the droplet has detached at $t = 0$. Given that the velocity magnitude increases linearly (except very close to impact at the T-shaped probe), the force field generated between the two microprobes to good approximation provides a constant acceleration g across the drop. Typical values for g in our experiments are 5–15 m/s^2. Applying this to the early stage of droplet deformation before detachment, we then fit the drop profile and extract the Bond number. An example is shown in Fig. 4(b) with a best-fit profile overlaid in red, corresponding to Bo = 0.24.

Figure 4(d) shows interfacial tension data from pendant drop experiments performed at different acoustic pressure values. Note that these p_{ac} are smaller than those cited for free floating droplets; the presence of the microprobes increases the local energy density near the droplet, while the p_{ac} values are derived from an empty acoustic cavity. As p_{ac} and, thus, the effective temperature increase, the interfacial tension determined from drop shape also increases, in contrast to typical liquids. We can rationalize this increase of line tension with effective temperature by recalling that attractive scattering forces and repulsive microstreaming forces both scale in the same way with sound energy density E_0 or, equivalently, sound pressure p_{ac} [Eq. (1)]. This means that the particle-particle interaction becomes stiffer while the particle separation remains fixed with increasing p_{ac}. As a result, despite the increased activity inside droplets at larger p_{ac}, their shape reflects a larger interfacial tension.

The scale of the line tension for our acoustically levitated liquid droplets is on the order of ∼10 nN. To compare to the surface tension of 3D liquids, we obtain an estimate by dividing γ by the particle diameter d. This gives a value of ∼0.25 mN/m. This is about 2 orders of magnitude lower than most ordinary liquids, but is comparable to liquid helium with ≈0.3 mN/m.

Viscosity. After the droplet "falls," it lands on the surface of the larger, T-shaped probe. It then spreads out and retracts in an oscillatory fashion before settling into a final shape. When it comes to rest, the sessile droplet appears hydrophilic due to its attraction to the probe. Images from the impact of the droplet in Fig. 4(b) are shown in Fig. 9, and Movie S2 of the Supplemental Material [29] shows an additional example. We can use this impact to estimate a value for the effective viscosity. Before impact, the droplet has kinetic and interfacial energy. As it lands and spreads out, it loses energy via viscous dissipation, and the interfacial energy changes with the drop shape. We compare the droplet's energy just before impact and at its maximum spread, which allows us to determine a value for the viscosity of a 2D droplet [46–48]. Details of this calculation can be found in Appendix E. Note that the units of dynamic viscosity η are different in 2D than in 3D, but the units of kinematic viscosity $\nu = \eta/\rho$ are the same. For this levitated granular droplet, we estimate $\nu \sim 1$ mm^2/s, which is very similar to the kinematic viscosity of water as well as to that of a 2D dusty plasma [49].

V. LIQUID PINCH-OFF

Tracking the breakup of liquid bridges under tension provides telltale signatures of both the material properties of the liquid and the forces controlling its state [50]. Therefore, this type of experiment offers another opportunity to assess to the effects of the emergent nonreciprocity that generates the liquidlike behavior in the droplets.

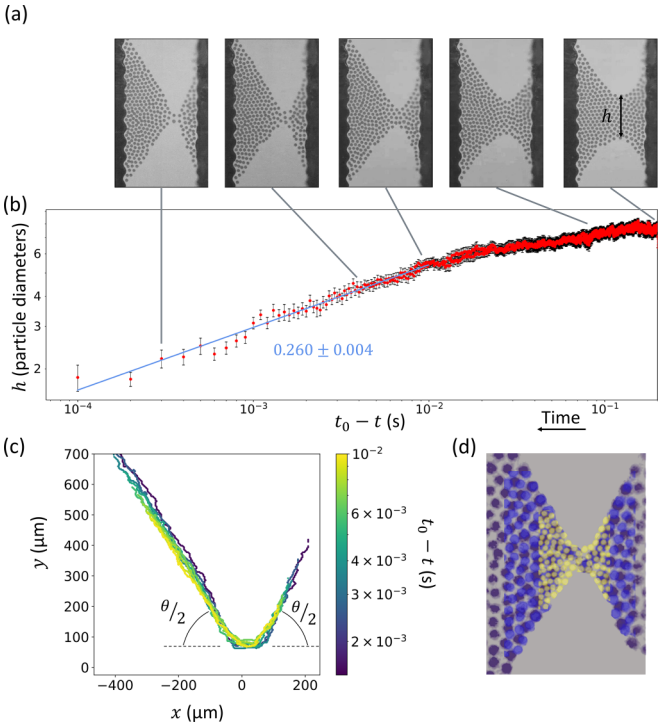


FIG. 5. Active granular liquid bridge pinch-off. (a) Time series of snapshots from high-speed video. (b) Ensemble average of neck width h vs time for all experiments; gray lines link the images to the corresponding times in the ensemble plot. Light blue line is a power law fit to the data on the left side of the plot. (c) Profiles of the neck, x and y scaled by power law relationship, at times within 10^{-2} s of pinch-off (colored by time). Cone half angles $\theta/2$ are drawn. (d) Overlaid images of neck profiles at three times, rescaled by power law relationship (colored by time).

In our experiments, levitating droplets were anchored to the faces of two opposing T-shaped microprobes. The configuration was similar to that in Fig. 4(a), except that the probe on the right (orange) was replaced by another T-shaped probe (black). Droplets were then stretched by moving one probe slowly (<50 μm/s) laterally until the liquid bridge pinched off. This pinch-off process is tracked by measuring the neck width h of the bridge as a function of time t up to pinch-off at t_0. Images from a representative experiment (see Movie S3 of the Supplemental Material [29]) are shown in Fig. 5(a): The dark bars on the left and right sides of each image are the ends of the T-shaped microprobes. The particles are attracted to the comparatively large faces of these two probes by forces due to scattered sound; indeed, as the panels in Fig. 5(a) show, the granular liquid very effectively "wets" those probes. By using a corrugated probe face, the contact angle remains fixed as tension is applied.

An ensemble average of neck width h versus time is plotted in Fig. 5(b). We performed 28 pinch-off experiments for various drop sizes and acoustic pressure levels, and averaged the value of $h(t)$ for each experiment; lines are drawn from the

snapshots of the experiment in panel (a) to the corresponding times in panel (b). Well before pinch-off, the thinning proceeds very slowly at a rate determined by the pulling speed. Approximately 0.01 s before pinch-off, or when the neck is close to $5d$ in width, the breakup speeds up. A fit to the ensemble-averaged data near pinch-off to a power law relationship of the form

$$h \sim (t_0 - t)^{\alpha} \tag{5}$$

gives an exponent of $\alpha = 0.260 \pm 0.004$ (if instead individual traces are fit separately, the mean scaling exponent is 0.28 ± 0.06; see Fig. 10).

Figure 5(c) shows profiles of the upper half of the neck in the 0.01 s before pinch-off [same experiment pictured in panel (a)]. The shape of the neck shows a double-cone mode with cone angle $\theta \approx 120°$–$150°$. Both the x and y dimensions of the profiles are scaled by a power law like Eq. (5) with $\alpha = 0.26$. The collapse of these profiles confirms that this stage of breakup is a self-similar process, and that the extent of the neck in the x direction scales similarly to the neck width with time. Figure 5(d) overlays images of the neck at three times, with colors corresponding approximately to the color bar in panel (c). These too mostly collapse onto one profile shape, with some slight variation in the center between the yellow profile (further from pinch-off) and the blue and purple (closer to pinch-off).

Self-similar power law scaling of the neck width near pinch-off is expected for ordinary liquids, where the exponent α reflects whether viscous, inertial, interfacial, or thermal effects dominate the pinch-off process [50]. This has been well studied for 3D systems, with exponents ranging from 1 for breakup dominated by viscous forces to 2/3 for the inviscid case to 0.418 for thermally driven breakup of nanojets [50] to 1/3 for breakup via chemical diffusion [51]. 2D liquid bridges, however, are fundamentally different. In particular, while interfacial tension in 3D acts to reduce the cylindrical radius at the narrowest point of the bridge, in 2D the effect of interfacial tension is to straighten out the neck boundary and thus *increase* its width [52]. Though interfacial tension can drive breakup in 2D, it occurs as a secondary effect resulting from the interfacial-tension-driven rebound of drop edges from an extended form [52], which gives a scaling exponent $\alpha \approx 0.7516$. In our experiments, this rebound cannot occur because the granular liquid bridges remain anchored to the two microprobes. Inertia and viscosity are typically not enough to drive breakup in an effectively 2D liquid sheet, instead requiring a contribution from vdW disjoining pressure or thermal gradients [53]. When vdW pressure is considered, it is predicted that a free-standing thin film can collapse with a scaling exponent as low as 2/7. However, in our experimental system, there is no true analog for vdW pressure between the interfaces of the neck. As a result, the data in Fig. 5(b) cannot be explained by existing scaling laws for pinch-off in 3D or 2D.

Fluctuation-driven pinch-off. The case where pinch-off behavior of a 3D liquid is dominated by the effects of thermal fluctuations seems to be the most similar case to the behavior we observe here. 2D liquid bridge breakup by thermal fluctuations, however, has so far not been explored systematically, and a corresponding exponent α is not known. Nevertheless, the characteristic double-cone shape observed in 3D liquid threads near pinch-off driven by strong thermal fluctuations [54,55] suggests that the double-cone-type pinch-off behavior we find [Fig. 5(a)] is also driven by fluctuations, although in this case the fluctuations arise as a consequence of emergent nonreciprocity.

Pinch-off and recoalescence. An unusual feature of this system is the potential for repeated pinch-off and coalescence. Depending on the experimental parameters, a bridge that pinches off due to particle fluctuations can reconnect, as shown in Fig. 6 and Movie S3 of the Supplemental Material [29]. During pinch-off experiments, the microprobe pulling the droplet apart moves very slowly relative to the particle motion. When the neck is reduced to a width of several particles, fluctuations of individual particles cause the neck to break. Particles retract to the edges of the remaining, smaller drops. However, the edges of the two droplet halves may still be just a few particle diameters apart. If particles from each half experience outward fluctuations, they can get close enough to reconnect the bridge. Other particles may then follow to again expand the neck to a width of several particles.

Attractive acoustic scattering forces extend over a longer distance than the repulsive forces from acoustic microstreaming, which decay exponentially. This difference is significant, and just after pinch-off there is still attraction between the two droplet halves. Combined with the low effective interfacial tension, this allows particles at the two facing perimeters to move across the gap, leading to recoalescence. Continuing active fluctuations then cause the liquid bridge to break up again.

This breakup and coalescence cycle can repeat multiple times, lasting until the two droplet halves are too far apart for their respective particles to form bridges. Several of these cycles are shown in Fig. 6(a), and a plot of the neck width versus time is shown in panel (b). This process exemplifies how the final pinch-off of the granular liquid bridges in this system is driven by particle fluctuations.

VI. CONCLUSION

Our results on acoustically levitated granular particles demonstrate that nonreciprocal, multibody interactions produce a liquid with unique traits. Increasing the interparticle force strength provokes an increase in particle kinetic energy, as the particle fluctuations are a consequence of the field-mediated interactions. Asymmetry within the spatial configuration of the particle ensemble gives rise to forces that facilitate particle motion; particles then move into another asymmetric configuration, which incites more motion, and so on. This phenomenon, enabled by nonreciprocal and multibody interactions, allows particles to move continuously and form a structure that resembles a liquid droplet. However, the behavior in this system is athermal, displaying long velocity distribution tails, superdiffusion, and collective motion, all of which are signatures of active and nonreciprocal systems. A pendant drop of such a liquid deforms similarly to a typical liquid under external stress, but its interfacial tension is low and increases with effective temperature; particles may be moving faster, but the bulk droplet is still bound more tightly. When this active liquid pinches off, the scaling of the neck width does not align with models of ordinary liquids, and

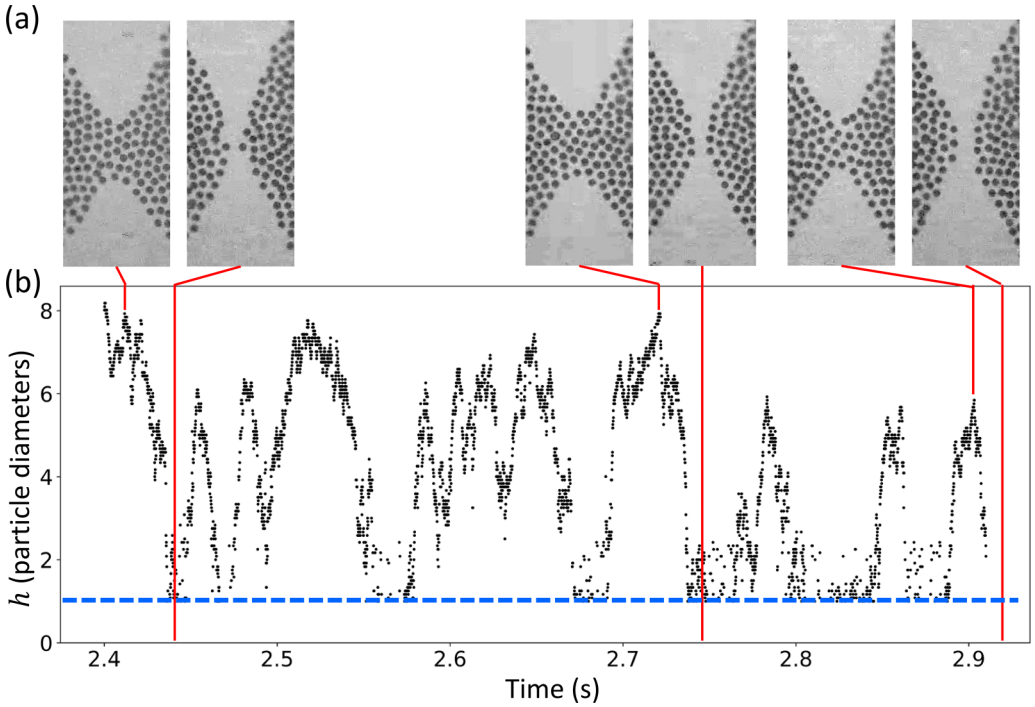


FIG. 6. An experimental granular droplet can pinch off and reconnect several times before it pinches off permanently. (a) A time series of images from the experiment. (b) Plot of neck width vs time for the end of the experiment where pinch-off and reconnection occur. Red lines connect images to times. Blue dashed line represents minimum neck width (one particle).

active, athermal fluctuations seem to dominate the behavior. These particle dynamics also enable a droplet to pinch off and reconnect spontaneously and cyclically. When particle activity is driven by strongly coupled interactions like these, enhanced activity does not drown out the strengthened effects of those complex interactions, but instead leads to phenomena unique to active liquids with nonreciprocal and multibody interactions. Future studies could examine more closely the nature of the solid-to-liquid transition in these systems by focusing on the evolution of defects as the solidlike configurations melt [30]. Furthermore, to better understand the role of higher-order N-body interactions in driving the activity in the liquid state observed by the experiments, advanced machine-learning-based approaches may prove useful.

ACKNOWLEDGMENTS

We thank Qinghao Mao, Brady Wu, Jochem Meijer, Alice Pelosse, and Billie Meadowcroft for inspiring discussions. We thank Jason Kronenfeld and Joe DeSimone for manufacturing the microprobe tips. This work was supported by the NSF through DMR-2104733. The experiments utilized the shared experimental facilities at the University of Chicago MRSEC, which is funded by the National Science Foundation under Award No. DMR-2011854. The research also benefited from computational resources and services supported by the Research Computing Center at the University of Chicago.

DATA AVAILABILITY

The data used to generate figures are available in Ref. [56].

APPENDIX A: ESTIMATING ACOUSTIC PRESSURE IN THE LEVITATION CAVITY

In a prior publication, we detailed a method for estimating the acoustic pressure in an acoustic levitation system [17]. We have improved upon this method by incorporating finite element analysis simulations.

A plane circular piston oscillating at a constant frequency produces a pressure field in free space with a maximum magnitude of $p_{\max} = 2\rho_0 c u_0$, where ρ_0 is the density of the medium (e.g., air), c is the sound speed, and u_0 is the oscillation speed. In our system, the bottom of the Langevin horn is akin to a circular piston. Thus, if we know the maximum pressure of a field produced by the horn in experiments, then we can determine the oscillation velocity and amplitude. We measure the sound pressure of our ultrasound source in free space. We remove the reflector from the experimental setup and replace it with absorbing foam several inches below the bottom of the horn. Then, we use a Xarion ETA100 optical microphone to measure the sound pressure $p_{\max} = 717$ Pa in free space for a frequency f_0 and input signal amplitude. We chose an input signal amplitude that is higher than that typically used for experiments to obtain less relative uncertainty in the pressure measurement. This results in a value for $u_0 = 0.852$ m/s, or an oscillation amplitude of $d_0 = 3.32$ μm.

We use COMSOL (Thermoviscous Acoustics module) to perform finite element analysis simulations of the system. We simulate a vibrating cylinder oscillating at f_0 with an amplitude of d_0 in an open box with absorbing walls. The maximum pressure of the acoustic field in this simulation is $p_{\max} \approx 730$ Pa, consistent with our experimental measurement.

We then simulate an acoustic cavity with a vibrating cylinder and a reflector. Using the same oscillation amplitude, we optimize the cavity height for f_0 and perform a frequency sweep. From this, we obtain values for $p_{\max} = 11\,300$ Pa and $p_{\text{avg}} = 1780$ Pa in the levitation plane. From the width of the pressure versus frequency curve, we determine the Q factor for the simulated cavity. We find $Q_{\text{sim}} \approx 250$, which is nearly $3\times$ larger than the quality factor for our experimental acoustic cavity of $Q_{\text{exp}} \approx 85$ [17].

The quality factor of the cavity should be proportional to the square of cavity pressure, so that $p^2_{\text{exp}} \approx (Q_{\text{exp}}/Q_{\text{sim}}) \cdot p^2_{\text{sim}}$. Thus, for an experimental cavity with the same horn oscillation amplitude d_0 and frequency f_0, but $Q = 85$, we can determine from the simulated values that $p_{\max} \approx 6540$ Pa and $p_{\text{avg}} \approx 1030$ Pa. As stated above, this is higher than the acoustic pressures used in these experiments. Finally, we use these values to calibrate the ultrasound sensors embedded in the experimental setup.

APPENDIX B: STRUCTURAL PARAMETERS

The local orientational order parameter ψ_6 is defined for a single particle j as

$$\psi_{6,j} = \frac{1}{n}\sum_{\ell} e^{6i\theta_\ell}, \tag{B1}$$

where the sum is over a particle's n nearest neighbors and θ_ℓ is the angle of the vector between particles j and ℓ. This is a complex vector quantity, where the magnitude suggests degree of crystallinity and the angle suggests crystal lattice orientation. To study trends of drop disorder with effective temperature, we compute $|\psi_6| = \langle|\psi_{6,j}|\rangle_j$ for particles in the interior of each droplet for each frame, and then time average $|\psi_6|$ over the course of the experiment.

The static structure factor $S(\mathbf{k})$ can be computed directly from particle positions as

$$S(\mathbf{k}) = \frac{1}{N}\left\langle \sum_{i=1}^{N}\sum_{j=1}^{N}[\cos(\mathbf{k}\cdot\mathbf{r}_i)\cos(\mathbf{k}\cdot\mathbf{r}_j) + \sin(\mathbf{k}\cdot\mathbf{r}_i)\sin(\mathbf{k}\cdot\mathbf{r}_j)]\right\rangle, \tag{B2}$$

where $\mathbf{r}_i$ is the position of particle i [57]. This calculation is performed by creating a 2D grid with spacing $2\pi/L$ (L: droplet diameter) and computing $S(\mathbf{k})$ for all $\mathbf{k} = (k_x, k_y)$ for each pair of particles. These values are averaged for each $k = |\mathbf{k}|$ to obtain $S(k)$. The radial distribution function $g(r)$ quantifies density correlations (or interparticle distances) in a sample. Figure 7 shows the radial distribution function $g(r)$ for levitated granular droplets at different kinetic energies; the x axis is r/σ, where σ is the mean interparticle spacing for the droplet in that experiment. The first peak represents the mean interparticle spacing. It is taller for the low KE experiments than for the high KE experiments, suggesting more structural order (more consistent interparticle spacing). Additionally, as r increases, the peak heights decay. For higher pressure samples, this decay is faster, and the peaks are closer to integer multiples of σ, suggesting a more isotropic structure. The

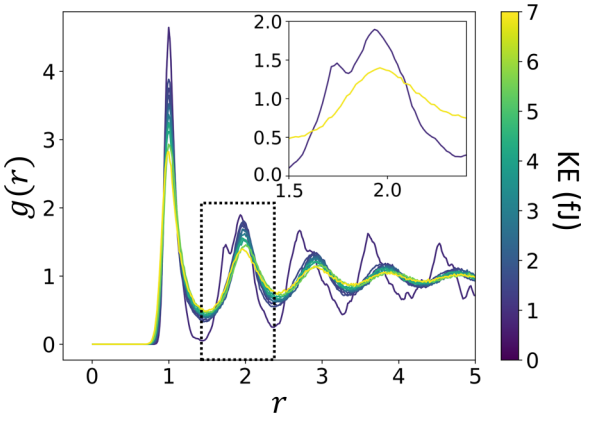


FIG. 7. Radial distribution function vs distance for experiments at different acoustic pressure values. Colors correspond to the color bar in Figs. 2(c) and 2(d). (Inset) $g(r)$ for the highest and lowest p_{ac} experiments, enlarged to the second peak.

inset of Fig. 1 shows $g(r)$ for the lowest (purple, 3880 Pa) and highest (yellow, 5920 Pa) p_{ac} experiments, enlarged to highlight the second peak [these experiments correspond to the images in Figs. 1(c) and 1(d), respectively, as well as Movie S1 of the Supplemental Material [29]]. For a perfect 2D solid crystal, the second peak of $g(r)$ splits into two subpeaks due to the two possible distances of particles in the second nearest neighbor shell [32,58]. The purple curve in Fig. 7(a) (inset) has a split second peak, indicating that it is in a solid state. The yellow curve is clearly rounded as expected for a liquid.

The radial distribution function is normally calculated as

$$g(r) = \frac{dn_r}{2\pi r dr \rho}, \tag{B3}$$

where n_r is the number of particles in a shell of thickness dr and ρ is the overall number density of the sample. Practically, this is computed by creating a histogram of all pairwise interparticle distances with bin size dr, and then dividing by the mean number of particles in a circular shell of radius r and thickness dr. Typically, for a liquid, $g(r) \to 1$ with increasing r. However, because these are small samples with a drop radius of $\approx$10 particle diameters and a defined boundary, calculating $g(r)$ with this method results in a function that decreases with r. This is due to incomplete shells at radius r for particles near the edge of the droplet. To avoid this, we compute $g(r)$ for each particle p_i in a frame. For a shell with radius r, instead of dividing by the total shell area $2\pi r dr$, we divide only by the area of the shell centered at p_i that actually overlaps the raft. We then average $g(r)$ for all particles within each frame, and time average $g(r)$ over the course of the experiment.

APPENDIX C: MOLECULAR DYNAMICS SIMULATIONS

To contrast with our acoustic experimental system, we performed molecular dynamics simulations of a thermal system with interparticle Coulomb repulsion and effective attraction via confinement. These simulations were performed with the HOOMD-blue package [59]. The simulation parameters were virtually identical to those described in the supplement of

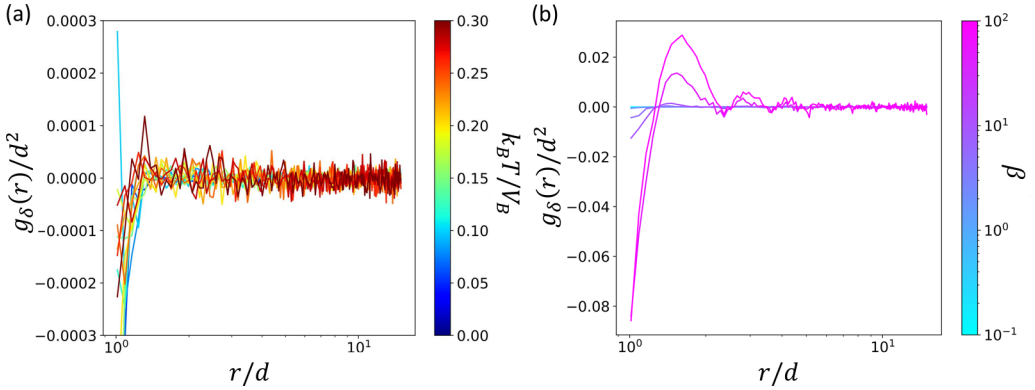


FIG. 8. Displacement correlations in MD simulations. (a) Displacement correlation function $g_\delta(r)$ vs r, varying simulation temperature with constant magnitudes of the interaction potentials. (b) Displacement correlation function $g_\delta(r)$ vs r, varying potential magnitudes and temperature together.

Ref. [15] for the simulation of a Wigner crystal, with a time step of 0.005 (simulation units). We chose these simulation potentials and parameters because, at low k_BT, they result in a system with an interior crystal and a round boundary, similar to acoustically levitated granular particles. We simulated 200 particles with diameter $D = 2^{1/6}$ in a 2D box with side length $L_{\text{Box}} = 300D$ with periodic boundary conditions. The potential

$$V_{\text{conf}}(r) = A \tanh\left[\frac{1}{2\pi pw}\cos\left(p\mathbf{b}_i \cdot \mathbf{r}\right)\right] \tag{C1}$$

confined particles to the center of the simulation box. For these simulations, $p = w = 1$, $b_i = 1/L_{\text{Box}}$, and $A = -10\tanh[(2\pi pw)^{-1}]$. This can be approximated as a radial harmonic potential close to the center of the box. The interparticle repulsion was a Yukawa potential

$$V_{\text{Yukawa}}(r) = \epsilon\frac{e^{-\kappa r}}{r}. \tag{C2}$$

Here, ϵ is an energy scale and κ is the reciprocal of a decay length; for these simulations, $\epsilon = 0.5$ and $\kappa = 1$.

We allowed the system to thermalize for 2 million time steps, and then continue the simulation for another 4 million time steps to obtain data for analysis. We varied the normalized temperature value applied as Langevin perturbations from 0 to 0.5 k_BT/V_B, where $V_B \approx 0.0418$ is the magnitude of the Yukawa potential at a distance of one lattice spacing. Prior work found that the system is melted for $k_BT/V_B > 0.1$. [15]. Note that the attraction applied here is solely from the global confinement potential, not interparticle attraction that depends directly on relative particle distances.

We then calculated the displacement correlation parameter g_δ [Eq. (3)] for each simulation. Figure 8(a) shows $g_\delta(r)$ versus r [comparable to Fig. 3(e)], with both axes normalized by particle diameter. While there may be slight correlation (or anticorrelation) at very small interparticle distances (when particles are nearly touching), this decays very quickly to zero. Changing the temperature does not substantially change this, though one should note that the magnitudes of the confining and repulsive potentials remained constant.

In the acoustic levitation experiments, the attractive and repulsive interactions and the particle kinetic energy all scale with cavity energy density (or pressure). We also simulated an analogous MD case in which the magnitudes of the confining and repulsive potentials were varied proportionally with the temperature. We multiplied the magnitudes of the confining and Yukawa potentials, as well as k_BT, by a parameter β. The k_BT/V_B value for these simulations was 0.2. Displacement correlations calculated from these simulations are shown in Fig. 8(b), with both axes normalized by particle diameter. The $g_\delta(r)$ versus r plot in panel (b) shows very little displacement correlation for small β. For large β, $g_\delta < 0$ when particles are very close, corresponding to the interparticle repulsion. $g_\delta(r)$ oscillates around 0 before tapering off at a distance of $\approx$4 particle diameters. Overall, these simulations do not suggest collective motion like that seen in the experiments.

APPENDIX D: TWO-DIMENSIONAL PENDANT DROP

For a 3D pendant drop, the Young-Laplace equation for a pendant drop is

$$\gamma\left(\frac{1}{R_1} + \frac{1}{R_2}\right) = \frac{2\gamma}{R_0} - \Delta\rho g z, \tag{D1}$$

where R_1 and R_2 are the radii of curvature at the surface, R_0 is the radius of the drop bulb, γ is the surface tension, and $\Delta\rho$ is the density difference between the inner and outer fluids (typically, some liquid and air). Note that hydrostatic pressure is given by $\Delta\rho g z$. We then parametrize the coordinates along the drop surface with parameter s that goes along the drop profile to obtain

$$\frac{dx}{ds} = \cos\varphi, \quad \frac{dz}{ds} = \sin\varphi, \quad \frac{1}{R_1} = \frac{d\varphi}{ds}, \quad \frac{1}{R_2} = \frac{\sin\varphi}{x}. \tag{D2}$$

Here, φ is the angle of a tangent line to the drop profile at a point, x is a radial coordinate, and z is an axial coordinate originating at the bottom center point of the drop. We nondimensionalize the equation (divide all length coordinates by R_0, e.g., $s \to \bar{s} = s/R_0$). Then, the differential equation for the drop shape can be written as

$$\frac{d\varphi}{d\bar{s}} = 2 - \frac{\Delta\rho g R_0^2}{\gamma}\bar{z} - \frac{\sin\varphi}{\bar{x}} = 2 - \text{Bo}\,\bar{z} - \frac{\sin\varphi}{\bar{x}}, \tag{D3}$$

with Bond number

$$\mathrm{Bo} = \frac{\Delta\rho g R_0^2}{\gamma}. \tag{D4}$$

In 2D, we only have one radius of curvature R_1 on the interface. We can write the Young-Laplace equation as

$$\frac{\gamma}{R_1} = \frac{\gamma}{R_0} - \Delta\rho g z, \tag{D5}$$

where γ is a line tension and $\Delta\rho$ is the area density difference. After doing the same coordinate parametrization, we get a simpler differential equation for the drop shape

$$\frac{d\varphi}{d\bar{s}} = 1 - \frac{\Delta\rho g R_0^2}{\gamma}\bar{z} = 1 - \mathrm{Bo}\,\bar{z}. \tag{D6}$$

Thus, the Bond number has the same expression, but the parameters in the expression have units corresponding to a 2D system.

In our system, the density of the particles is $\rho_p \simeq 1000\,\mathrm{kg/m^3}$. Using the number of particles and raft radius from the floating droplet experiments in the main text, we compute an area density for the raft of $\rho_{r,\mathrm{area}} \approx 0.0133\,\mathrm{kg/m^2}$. We fit the drop interface curves as solutions to the differential equation, find the Bond number, and plug in experimental values to determine the interfacial tension of the droplets.

APPENDIX E: ESTIMATING VISCOSITY

We use an energy balance to estimate the viscosity μ of a 2D droplet that has impacted a surface. Note that in 2D, dynamic viscosity has units of kg/s, in contrast to a 3D system where it has units of kg/(m s). We follow Refs. [48] and [47], which perform an analogous calculation for a 3D droplet. Suppose the diameter of the falling circular droplet is D_0, and assume that after landing with impact velocity V_i the droplet spreads into a rectangular shape with diameter D and thickness h. While falling, the droplet has energy that is a sum of kinetic energy

$$\mathrm{KE}_i = \frac{1}{2}mV_i^2 = \frac{\pi\rho}{8}D_0^2V_i^2, \tag{E1}$$

where ρ is the area density of the droplet, and interfacial energy

$$\mathrm{IE}_i = \pi D_0\gamma, \tag{E2}$$

where γ is the interfacial (line) tension, as measured in the pendant drop experiments in the main text.

After landing, the drop has interfacial energy

$$\mathrm{IE}_f = S_{\mathrm{LV}}\gamma + S_{\mathrm{SL}}(\gamma_{\mathrm{SL}} - \gamma_{\mathrm{SV}}), \tag{E3}$$

where S_{LV} is the liquid-vapor (droplet-air) interface length, S_{SL} is the liquid-solid (droplet-probe) interface length, and γ_{SL} and γ_{SV} are the solid-liquid and solid-vapor interfacial tension values, respectively. At its maximum spreading diameter $D_{\max}$, assume that the droplet is at rest, so that the remainder of the initial energy has gone to viscous dissipation

$$W \approx \tau\Omega t_{\max}, \tag{E4}$$

where τ is the energy dissipated per area per time, written as $\tau \approx \mu(V_i/\delta)^2$, Ω is the area over which the viscous dissipation takes place, expressed as $\Omega = D_{\max}\delta$, and $t_{\max}$ is the time it takes for the drop to spread to its maximum radius. Then, δ is the depth that momentum can diffuse in the droplet while the drop is moving, written as $\delta = \sqrt{cD_\mu t_{\max}}$, where $D_\mu = \mu/\rho$ is the transverse momentum diffusion constant and c is a constant that is of order 1.

We can use Young's equation to simplify the equation for IE_f. Take θ to be the contact angle of the drop. Then,

$$\begin{aligned} \gamma_{\mathrm{SV}} &= \gamma_{\mathrm{SL}} + \gamma\cos\theta, \\ \gamma_{\mathrm{SL}} - \gamma_{\mathrm{SV}} &= -\gamma\cos\theta, \\ \mathrm{IE}_f &= S_{\mathrm{LV}}\gamma - S_{\mathrm{SL}}\gamma\cos\theta. \end{aligned} \tag{E5}$$

Using the static or dynamic contact angle θ does not substantially change the final result for our purpose, which is to obtain an estimate of the viscosity. Assuming an approximately rectangular shape of the maximally spread droplet, $S_{\mathrm{LV}} = D_{\max} + 2h$ and $S_{\mathrm{SL}} = D_{\max}$. We can compute a value for h assuming volume (area) conservation of the droplet before and after impact:

$$\pi D_0^2 = hD_{\max} \Rightarrow h = \frac{\pi D_0^2}{D_{\max}}. \tag{E6}$$

Now, we write the interfacial energy at maximum spread as

$$\mathrm{IE}_f = D_{\max}\gamma(1 - \cos\theta) + 2\pi\gamma\frac{D_0^2}{D_{\max}}. \tag{E7}$$

The remaining unknown quantity is $t_{\max}$. To compute this, we follow Ref. [46]. While the drop is midimpact, suppose it is composed of a truncated circular portion (diameter D_0, truncated line length ℓ) moving toward the impact surface at V_i, and a rectangular portion (diameter D, height h) with radial velocity V_R. Then, by volume (area) conservation, the area of liquid exiting the truncated sphere over a time t must equal the area that the cylinder expands by in that same time, so

$$\begin{aligned} \Delta A_{\mathrm{circ}} &= \Delta A_{\mathrm{rect}}, \\ \ell V_i t &= hV_R t, \\ \frac{V_R}{V_i} &= \frac{\ell}{h} = \frac{\ell D_{\max}}{\pi D_0^2}. \end{aligned} \tag{E8}$$

Assume $\ell \sim \frac{D_0}{2}$. Then, we can examine how D changes in time:

$$2V_R = \frac{dD}{dt} = \frac{D_{\max}}{\pi D_0}V_i \Rightarrow \frac{D}{D_{\max}} = \frac{V_i}{\pi D_0}t. \tag{E9}$$

When $D = D_{\max}$, then

$$1 = \frac{V_i}{\pi D_0}t_{\max} \Rightarrow t_{\max} = \frac{\pi D_0}{V_i}. \tag{E10}$$

Combining all of this, we can write $\delta = \sqrt{\frac{2\pi\mu D_0}{\rho V_i}}$, $\tau = \frac{\rho V_i^3}{2\pi D_0}$, and $\Omega = D_{\max}\sqrt{\frac{2\pi\mu D_0}{\rho V_i}}$. We substitute these expressions into our viscous dissipation term:

$$W = D_{\max}\sqrt{\frac{\pi\mu\rho D_0 V_i^3}{c}}. \tag{E11}$$

Finally, we write the full energy balance equation and then solve for μ:

$$\mathrm{KE}_i + \mathrm{IE}_i = W + \mathrm{IE}_f,$$

$$\frac{\pi}{8}\rho D_0^2 V_i^2 + \pi D_0 \gamma = D_{\max}\sqrt{\frac{\pi\mu\rho D_0 V_i^3}{c}} + D_{\max}\gamma(1-\cos\theta) + 2\pi\gamma\frac{D_0^2}{D_{\max}},$$

$$\mu = \frac{c\left(\gamma D_{\max}^2(\cos\theta - 1) + 8\gamma D_0(D_{\max} - 2D_0) + \pi\rho D_0^2 D_{\max} V_i^2\right)^2}{32\pi\rho D_0 D_{\max}^4 V_i^3}. \tag{E12}$$

To compute a value for μ, we use experimental values from the pendant drop experiment shown in Figs. 4(b) and 4(c) and Fig. 9 (which shows drop impact and spreading): $\gamma \sim 10$ nN, $D_0 \sim 500$ μm, $D_{\max} \sim 2000$ μm, $\rho \sim 0.01\,\mathrm{kg/m^2}$, $V_i \sim 0.05$ m/s, $\theta \sim 30°$, and the literature value of $c \approx 2$. This gives a dynamic viscosity of

$$\mu \sim 10^{-8}\ \mathrm{kg/s}.$$

Note the units: This is for a 2D system. However, the kinematic viscosity $\nu = \mu/\rho$ has the same units for 2D and 3D liquids. The kinematic viscosity of this system is

$$\nu = \frac{\mu}{\rho} \sim \frac{10^{-8}}{0.01} \approx 10^{-6}\ \mathrm{m^2/s} \Rightarrow \nu \sim 1\ \mathrm{mm^2/s}, \tag{E13}$$

which is similar to that of water.

This calculation has assumed that the interfacial tension of a hanging drop is a constant equal to the tension of the drop once it is sessile. This may not be accurate, as the force field immediately next to the larger T-shaped probe has an increased local energy density and a significant force gradient. We also assume area conservation of the droplet throughout impact and rebound. In addition, the constant c in the expression for the diffusion depth δ varies in different 3D models but is typically between 1 and 2; we expect it to be somewhat similar for 2D. We believe that discrepancies caused by these assumptions do not significantly impact the order-of-magnitude estimate for viscosity.

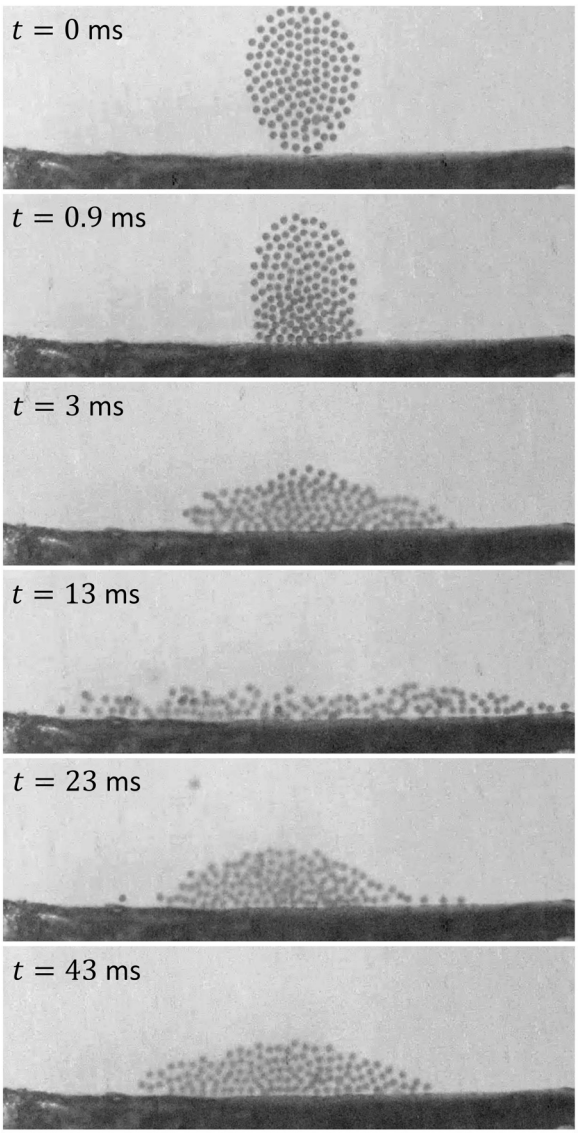


FIG. 9. Time series of images showing a levitated granular droplet impacting the surface of a microprobe. Filmed at 10 000 FPS. ($t = 0$ ms) Droplet just before impact. ($t = 0.9$ ms) Droplet makes contact with probe surface. ($t = 3$ ms) Droplet spreads on probe. ($t = 13$ ms) Droplet spreads to maximum width. ($t = 23$ ms) Droplet rebounds to a rounder shape. ($t = 43$ ms) Droplet settles into final sessile shape.

APPENDIX F: PINCH-OFF SCALING

As described in the main text, we performed 28 pinch-off experiments of this granular liquid. We fit neck width h versus

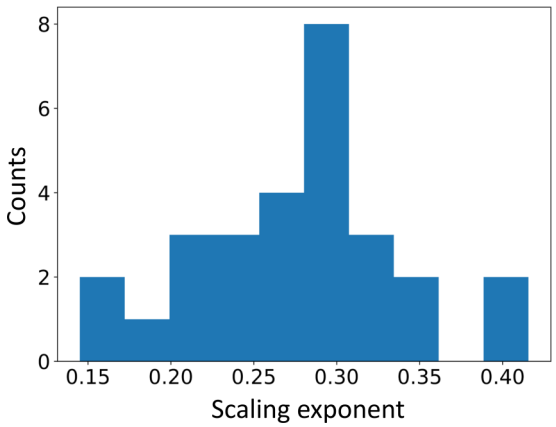


FIG. 10. Histogram of best-fit scaling exponents α for individual drop pinch-off experiments.

time to pinch-off $t_0 - t$ to a power law with exponent α for each individual experiment and obtained the distribution in Fig. 10. This gives a mean scaling exponent of $\alpha = 0.28 \pm 0.06$.

[1] M. Fruchart and V. Vitelli, Nonreciprocal many-body physics, arXiv:2602.11111.

[2] A. Dinelli, J. O'Byrne, A. Curatolo, Y. Zhao, P. Sollich, and J. Tailleur, Non-reciprocity across scales in active mixtures, Nat. Commun. **14**, 7035 (2023).

[3] M. Fruchart, R. Hanai, P. B. Littlewood, and V. Vitelli, Non-reciprocal phase transitions, Nature (London) **592**, 363 (2021).

[4] M. C. Marchetti, J. F. Joanny, S. Ramaswamy, T. B. Liverpool, J. Prost, M. Rao, and R. A. Simha, Hydrodynamics of soft active matter, Rev. Mod. Phys. **85**, 1143 (2013).

[5] E. M. King, M. C. Morrell, J. B. Sustiel, M. Gronert, H. Pastor, and D. G. Grier, Scattered waves fuel emergent activity, Phys. Rev. Res. **7**, 013055 (2025).

[6] L. S. Matthews, D. L. Sanford, E. G. Kostadinova, K. S. Ashrafi, E. Guay, and T. W. Hyde, Dust charging in dynamic ion wakes, Phys. Plasmas **27**, 023703 (2020).

[7] W. Yu, E. Abdelaleem, I. Nemenman, and J. C. Burton, Physics-tailored machine learning reveals unexpected physics in dusty plasmas, Proc. Natl. Acad. Sci. USA **122**, e2505725122 (2025).

[8] Z. Shu, W.-C. Li, W. Yu, and J. C. Burton, Nonreciprocal interactions drive intermittent melting of Coulomb clusters, Newton **2**, 100633 (2026).

[9] A. V. Zampetaki, B. Liebchen, A. V. Ivlev, and H. Löwen, Collective self-optimization of communicating active particles, Proc. Natl. Acad. Sci. USA **118**, e2111142118 (2021).

[10] D. J. Davenport and D. Kleckner, Formation of colloidal chains and driven clusters with optical binding, Soft Matter **18**, 4464 (2022).

[11] X. Li, Y. Liu, Z. Lin, J. Ng, and C. T. Chan, Non-Hermitian physics for optical manipulation uncovers inherent instability of large clusters, Nat. Commun. **12**, 6597 (2021).

[12] J. Parker, S. Nagasamudram, C. Peterson, Y. Li, S. Soleimanikahnoj, S. A. Rice, and N. F. Scherer, Symmetry breaking-induced N-body electrodynamic forces in optical matter systems, Nat. Commun. **16**, 6294 (2025).

[13] N. S. Clair, D. Davenport, A. D. Kim, and D. Kleckner, Dynamics of acoustically bound particles, Phys. Rev. Res. **5**, 013051 (2023).

[14] M. C. Morrell, L. Elliott, and D. G. Grier, Nonreciprocal wave-mediated interactions power a classical time crystal, Phys. Rev. Lett. **136**, 057201 (2026).

[15] B. Wu, B. VanSaders, M. X. Lim, and H. M. Jaeger, Hydrodynamic coupling melts acoustically levitated crystalline rafts, Proc. Natl. Acad. Sci. USA **120**, e2301625120 (2023).

[16] B. Wu, Q. Mao, B. VanSaders, and H. M. Jaeger, Nonreciprocity and multibody interactions in acoustically levitated particle systems: A three-body problem, Phys. Rev. E **112**, 035410 (2025).

[17] N. M. Brown, B. VanSaders, J. M. Kronenfeld, J. M. DeSimone, and H. M. Jaeger, Direct measurement of forces in air-based acoustic levitation systems, Rev. Sci. Instrum. **95**, 094901 (2024).

[18] N. M. Brown, B. VanSaders, J. M. Kronenfeld, J. M. DeSimone, and H. M. Jaeger, Tunable mechanical properties and air-based lubrication in an acoustically levitated granular material, Granular Matter **27**, 20 (2025).

[19] M. X. Lim, B. VanSaders, and H. M. Jaeger, Acoustic manipulation of multi-body structures and dynamics, Rep. Prog. Phys. **87**, 064601 (2024).

[20] J. Rudnick and M. Barmatz, Oscillational instabilities in single-mode acoustic levitators, J. Acoust. Soc. Am. **87**, 81 (1990).

[21] M. X. Lim, A. Souslov, V. Vitelli, and H. M. Jaeger, Cluster formation by acoustic forces and active fluctuations in levitated granular matter, Nat. Phys. **15**, 460 (2019).

[22] M. A. B. Andrade, F. Buiochi, and J. C. Adamowski, Finite element analysis and optimization of a single-axis acoustic levitator, IEEE Trans. Ultrason. Ferroelectr. Freq. Control **57**, 469 (2010).

[23] B. Wu, E. P. Esposito, Q. Mao, and H. M. Jaeger, Pattern formation in acoustically levitated particle systems with competing near-field interactions, Phys. Rev. Res. **7**, 023017 (2025).

[24] K. Hsiao, B. J. Lee, T. Samuelsen, G. Lipkowitz, J. M. Kronenfeld, D. Ilyn, A. Shih, M. T. Dulay, L. Tate, E. S. G. Shaqfeh, and J. M. DeSimone, Single-digit-micrometer-resolution continuous liquid interface production, Sci. Adv. **8**, eabq2846 (2022).

[25] A. Kirillov, E. Mintun, N. Ravi, H. Mao, C. Rolland, L. Gustafson, T. Xiao, S. Whitehead, A. C. Berg, W.-Y. Lo, P. Dollár, and R. Girshick, Segment anything, arXiv:2304.02643.

[26] J. C. Crocker and D. G. Grier, Methods of digital video microscopy for colloidal studies, J. Colloid Interface Sci. **179**, 298 (1996).

[27] J. D. Berry, M. J. Neeson, R. R. Dagastine, D. Y. C. Chan, and R. F. Tabor, Measurement of surface and interfacial tension using pendant drop tensiometry, J. Colloid Interface Sci. **454**, 226 (2015).

[28] E. Huang, A. Skoufis, T. Denning, J. Qi, R. R. Dagastine, R. F. Tabor, and J. D. Berry, OpenDrop: Open-source software for pendant drop tensiometry contact angle measurements, J. Open Source Software **6**, 2604 (2021).

[29] See Supplemental Material at http://link.aps.org/supplemental/10.1103/vdq4-r1cc for videos of experiments.

[30] A. D. Vyas, P. W. A. Schönhöfer, T. M. Hopkins, A. D. Hollingsworth, S. Sacanna, S. C. Glotzer, and P. Chaikin, Two-dimensional non-equilibrium melting of charged colloids, Nat. Phys. **22**, 287 (2026).

[31] J.-P. Hansen and L. Verlet, Phase transitions of the Lennard-Jones system, Phys. Rev. **184**, 151 (1969).

[32] Z. Wang, A. M. Alsayed, A. G. Yodh, and Y. Han, Two-dimensional freezing criteria for crystallizing colloidal monolayers, J. Chem. Phys. **132**, 154501 (2010).

[33] J. M. Caillol, D. Levesque, J. J. Weis, and J. P. Hansen, A Monte Carlo study of the classical two-dimensional one-component plasma, J. Stat. Phys. **28**, 325 (1982).

[34] S. Ranganathan and K. N. Pathak, Freezing transition of two-dimensional Lennard-Jones fluids, Phys. Rev. A **45**, 5789 (1992).

[35] V. Zhuravlyov, J. Goree, P. Elvati, and A. Violi, Finite-size effects in the static structure factor $S(k)$ and $S(0)$ for a two-dimensional Yukawa liquid, Phys. Rev. E **108**, 035211 (2023).

[36] T. van Noije and M. Ernst, Velocity distributions in homogeneous granular fluids: The free and the heated case, Granular Matter **1**, 57 (1998).

[37] F. Rouyer and N. Menon, Velocity fluctuations in a homogeneous 2D granular gas in steady state, Phys. Rev. Lett. **85**, 3676 (2000).

[38] V. V. Prasad, D. Das, S. Sabhapandit, and R. Rajesh, Velocity distribution of driven granular gases, J. Stat. Mech. (2019) 063201.

[39] A. Barrat and E. Trizac, Random inelasticity and velocity fluctuations in a driven granular gas, Eur. Phys. J. E **11**, 99 (2003).

[40] T. Demaerel, W. De Roeck, and C. Maes, Producing suprathermal tails in the stationary velocity distribution, Phys. A: Stat. Mech. Appl. **552**, 122179 (2020).

[41] Y.-F. Chen, H.-H. Wei, Y.-J. Sheng, and H.-K. Tsao, Superdiffusion in dispersions of active colloids driven by an external field and their sedimentation equilibrium, Phys. Rev. E **93**, 042611 (2016).

[42] H. E. Ribeiro and F. Q. Potiguar, Active matter in lateral parabolic confinement: From subdiffusion to superdiffusion, Phys. A: Stat. Mech. Appl. **462**, 1294 (2016).

[43] G. Ariel, A. Rabani, S. Benisty, J. D. Partridge, R. M. Harshey, and A. Be'er, Swarming bacteria migrate by Lévy Walk, Nat. Commun. **6**, 8396 (2015).

[44] W.-T. Juan and L. I, Anomalous diffusion in strongly coupled quasi-2D dusty plasmas, Phys. Rev. Lett. **80**, 3073 (1998).

[45] B. R. Andrew, L. Guazzotto, L. Matthews, T. Hyde, and E. G. Kostadinova, Anisotropic anomalous diffusion in microgravity dusty plasma. I. Nonextensive statistical analysis, Phys. Plasmas **32**, 103702 (2025).

[46] M. Pasandideh-Fard, Y. M. Qiao, S. Chandra, and J. Mostaghimi, Capillary effects during droplet impact on a solid surface, Phys. Fluids **8**, 650 (1996).

[47] T. Mao, D. C. S. Kuhn, and H. Tran, Spread and rebound of liquid droplets upon impact on flat surfaces, AIChE J. **43**, 2169 (1997).

[48] J. B. Lee, D. Derome, R. Guyer, and J. Carmeliet, Modeling the maximum spreading of liquid droplets impacting wetting and nonwetting surfaces, Langmuir **32**, 1299 (2016).

[49] V. Nosenko and J. Goree, Shear flows and shear viscosity in a two-dimensional Yukawa system (dusty plasma), Phys. Rev. Lett. **93**, 155004 (2004).

[50] J. Eggers and E. Villermaux, Physics of liquid jets, Rep. Prog. Phys. **71**, 036601 (2008).

[51] H. Y. Lo, Y. Liu, S. Y. Mak, Z. Xu, Y. Chao, K. J. Li, H. C. Shum, and L. Xu, Diffusion-dominated pinch-off of ultralow surface tension fluids, Phys. Rev. Lett. **123**, 134501 (2019).

[52] J. C. Burton and P. Taborek, Two-dimensional inviscid pinch-off: An example of self-similarity of the second kind, Phys. Fluids **19**, 102109 (2007).

[53] H. Wee, A. H. Kumar, X. Liu, and O. A. Basaran, Escape from pinch-off during contraction of liquid sheets and two-dimensional drops of low-viscosity fluids, Phys. Rev. Fluids **9**, 103601 (2024).

[54] M. Moseler and U. Landman, Formation, stability, and breakup of nanojets, Science **289**, 1165 (2000).

[55] J. Eggers, Dynamics of liquid nanojets, Phys. Rev. Lett. **89**, 084502 (2002).

[56] N. M. Brown and H. M. Jaeger, Nonreciprocal multi-body interactions activate liquid state of acoustically levitated particle ensembles, Materials Data Facility (2026), DOI: 10.18126/qdd1-5644.

[57] A. L. Thorneywork, S. K. Schnyder, D. G. A. L. Aarts, J. Horbach, R. Roth, and R. P. A. Dullens, Structure factors in a two-dimensional binary colloidal hard sphere system, Mol. Phys. **116**, 3245 (2018).

[58] T. M. Truskett, S. Torquato, S. Sastry, P. G. Debenedetti, and F. H. Stillinger, Structural precursor to freezing in the hard-disk and hard-sphere systems, Phys. Rev. E **58**, 3083 (1998).

[59] J. A. Anderson, J. Glaser, and S. C. Glotzer, HOOMD-blue: A Python package for high-performance molecular dynamics and hard particle Monte Carlo simulations, Comput. Mater. Sci. **173**, 109363 (2020).